UNIVERSITY *of York*

This is a repository copy of *Lipid metabolic perturbation is an early-onset phenotype in adult spinster mutants: a Drosophila model for lysosomal storage disorders*.

White Rose Research Online URL for this paper:
https://eprints.whiterose.ac.uk/126080/

Version: Published Version

Article:

White Rose
university consortium
Universities of Leeds, Sheffield & York

eprints@whiterose.ac.uk
https://eprints.whiterose.ac.uk/

Lipid metabolic perturbation is an early-onset phenotype in adult *spinster* mutants: a *Drosophila* model for lysosomal storage disorders

Sarita Hebbar[a,†,*], Avinash Khandelwal[a,‡], R. Jayashree[b], Samantha J. Hindle[c,§], Yin Ning Chiang[d], Joanne Y. Yew[e], Sean T. Sweeney[c,*], and Dominik Schwudke[a,‖,*]
[a]National Center for Biological Sciences, Tata Institute for Fundamental Research, Bangalore 560065, India; [b]Centre for Cellular and Molecular Platforms (C-CAMP), Proteomics Facility, Bangalore 560065, India; [c]Department of Biology, University of York, York YO10 5DD, UK; [d]Temasek Life Sciences Laboratory, Singapore 117604; [e]Pacific Biosciences Research Center, University of Hawai'i at Mānoa, Honolulu, HI 96822

ABSTRACT Intracellular accumulation of lipids and swollen dysfunctional lysosomes are linked to several neurodegenerative diseases, including lysosomal storage disorders (LSD). Detailed characterization of lipid metabolic changes in relation to the onset and progression of neurodegeneration is currently missing. We systematically analyzed lipid perturbations in *spinster (spin)* mutants, a *Drosophila* model of LSD-like neurodegeneration. Our results highlight an imbalance in brain ceramide and sphingosine in the early stages of neurodegeneration, preceding the accumulation of endomembranous structures, manifestation of altered behavior, and buildup of lipofuscin. Manipulating levels of *ceramidase* and altering these lipids in *spin* mutants allowed us to conclude that ceramide homeostasis is the driving force in disease progression and is integral to *spin* function in the adult nervous system. We identified 29 novel physical interaction partners of Spin and focused on the lipid carrier protein, Lipophorin (Lpp). A subset of Lpp and Spin colocalize in the brain and within organs specialized for lipid metabolism (fat bodies and oenocytes). Reduced Lpp protein was observed in *spin* mutant tissues. Finally, increased levels of lipid metabolites produced by oenocytes in *spin* mutants allude to a functional interaction between Spin and Lpp, underscoring the systemic nature of lipid perturbation in LSD.

INTRODUCTION

Abnormal lipid metabolism and lipid accumulation are hallmarks of neurodevelopmental and neurodegenerative disorders. Through detailed mass spectrometry studies, perturbations in lipid metabolism have been reported (Cutler *et al.*, 2004; Han *et al.*, 2011; Cheng *et al.*, 2013; Panchal *et al.*, 2014). But a systematic analysis through disease onset and progression has not yet been possible. With the help of recently established high-throughput lipidomics platforms (Shevchenko and Simons, 2010; Schwudke *et al.*, 2011), rapid and

Abbreviations used: Akt, protein kinase-B; ApoLpp, apolipophorin; CBR, cell body rind; CerPE, ceramide phosphotidylethanolamine; CHC, cuticular hydrocarbons; co-IP, coimmunoprecipitation; EI, electron ionization; GCMS, gas chromatography mass spectrometry; GFP, green fluorescent protein; LC-MS, liquid chromatography–mass spectrometry; Lpp, lipophorin; LSD, lysosomal storage disorder; MAPK, mitogen-activated protein kinase; MTBE, methyl tert-butyl ether; PC, phosphatidylcholine; PE, phosphatidylethanolamine; PE-O, phosphatidylethanolamine ether; PI, phosphatidylinostiol; ROS, reactive oxygen species; S1P, sphingosine-1-phosphate; SBB, Sudan-Black-B; Sph, sphingosine; TEM, transmission electron microscopy.

quantitative analyses of lipids are now feasible for complex and large studies. This has been especially useful for the characterization of lipidomes of routinely used biological model systems such as human cell lines (Sampaio *et al.*, 2011), yeast (Ejsing *et al.*, 2009), and *Drosophila melanogaster*. In the context of *Drosophila*, an extensively used model system, detailed lipidomics resources are now available with a focus on development and nutrition (Carvalho *et al.*, 2010, 2012; Guan *et al.*, 2013). The fly lipidome is distinct from its mammalian counterpart in many aspects, including that the major sterol is not cholesterol but ergosterol. In flies, the main membrane phospholipid is phosphatidylethanolamine (PE) and not phosphatidylcholine (PC), and the most abundant sphingolipid is ceramide phosphotidylethanolamine (CerPE), which substitutes an ethanolamine group for the choline group found in mammalian sphingomyelins (Carvalho *et al.*, 2012). The sphingoid base chain length of *Drosophila* sphingolipids is shorter (predominantly C14) than in the mammalian system (C18). Typically, there are no polyunsaturated fatty acids (such as 20:4/20:5/22:5/22:6) present in *Drosophila*. Glycosphingolipids in flies are constituted by a core of mannose-glucosyl ceramide as opposed to galactose-glucosyl ceramide in mammals. Interestingly, none of the reported glycosphingolipids are sialylated as in mammals but instead have an N-acetyl-glucosyl head group (Seppo *et al.*, 2000). Although gangliosides have not been described in *Drosophila*, orthologues of genes involved in ganglioside (GM2 and GM3) metabolism occur in the fly genome (Stern *et al.*, 2000; Starostina *et al.*, 2009). Despite these differences, many mammalian genes for lipid metabolism and transport are functionally conserved in *Drosophila*, suggesting common principles in their metabolism and transport (Hortsch *et al.*, 2010). Furthermore, many relevant human disease associated genes connected to lipid metabolism and transport are functionally conserved; these include *Taz*, involved in mitochondrial lipid remodeling (Barth syndrome; (Xu *et al.*, 2006); *Cerk*, regulating ceramide metabolism (retinitis pigmentosa (Dasgupta *et al.*, 2009); as well as *dnpc1* and *dnpc2*, critical for lipid transport and *dsap-r*, the *pro-saposin* ortholog for sphingolipid metabolism (Hindle *et al.*, 2017), in addition to many genes involved in lysosomal storage disorders; reviewed in Hindle *et al.* (2011).

Using the advancements in lipidomics, we aim to understand the nature of lipid perturbations in disease onset and progression. Contrary to other disease models or patient samples, systematic and kinetic studies on lipids are relatively easily carried out in *Drosophila*, which is a well-accepted animal model for human disease (Bilen and Bonini, 2005). We focused on fly *spinster (spin)* mutants, which exhibit neurodegeneration with lysosomal storage disorders (LSD)-like features (Nakano *et al.*, 2001; Sweeney and Davis, 2002; Dermaut *et al.*, 2005; Hindle *et al.*, 2011). Lipid metabolic changes in *spin* mutants have not been characterized despite their established link to neurodegeneration and their use as genetic tool to perturb sphingolipid levels (Osborne *et al.*, 2008; Pantoja *et al.*, 2013; Sasamura *et al.*, 2013).

We have systematically analyzed and quantified lipids in adult *spin* brains at specific stages of disease onset and progression using lipidomics approaches while simultaneously describing the overall integrity of the nervous system using imaging, behavior, and lifespan analyses. Our experiments have helped establish a time line of events that place loss of *spin* function before the ceramide metabolic imbalance in the progression of disease. Using proteomics approaches coupled with pull-down assays, we have compiled a resource list of Spinster (Spin) interactor proteins. For one of these, Lipophorin (Lpp), we present an interesting possibility that loss of Spin also causes a more general effect with changes in other lipid metabolites in tissues that regulate lipid metabolism (oenocytes).

RESULTS

Spin encodes a transmembrane protein that localizes to the late endolysosomal compartments. Early phenotypes associated with *spin* mutants include reduced viability and morphological abnormalities at the larval neuromuscular synapses and enlarged lysosomes (Sweeney and Davis, 2002). Typically, LSD are among the most common childhood neurodegenerative diseases (Hindle *et al.*, 2011), and this is reflected in the shortened life span and reduced mobility of young *spin* mutant flies (Nakano *et al.*, 2001; Dermaut *et al.*, 2005). A hallmark of *spin* mutant brains is their characteristic autofluorescence, which is attributed to lipofuscin or the ageing pigment (Nakano *et al.*, 2001). It is a mixture of accumulated/unmetabolized lipids and proteins and is distinguished by autofluorescence in ageing and degenerating tissues (Gray and Woulfe, 2005). Related to this, adult *spin* mutant brains, retinas, and the larval neuromuscular synapse exhibit an accumulation of electron dense material and membrane whorls (Nakano *et al.*, 2001; Dermaut *et al.*, 2005).

Increased ceramide levels and lipofuscin in *spin* mutant brains

We imaged dissected adult brains for lipofuscin (recognized by its autofluorescence properties) and subsequently performed lipidomics on the imaged brains. To define the time course of lipofuscin accumulation and lipid profile alterations, we dissected brains at 1, 2, 4 and 8 d after eclosion. Our image analyses confirmed that *spin* mutant brains exhibit increased autofluorescence (Figure 1Ai), which is an indication of lipofuscin (Nakano *et al.*, 2001; Venkatachalam *et al.*, 2008). In contrast, age-matched controls showed no autofluorescence whatsoever (Figure 1Ai). The heteroallelic combination *spin⁴/spin⁵* was used; it displays strong *spin*-associated phenotypes for viability and synapse morphology (Sweeney and Davis, 2002) and only a limited number of escapers are viable until adulthood. These escaper adults have a reduced lifespan (Supplemental Figure 1).

Using phalloidin as a general marker of brain volume, the autofluorescence in the green channel is used as an indicator of lipofuscin. In a maximum intensity projection of the mutant brain, lipofuscin-rich regions are visible in the entire brain (green channel; Figure 1Aii). There is no pattern in the spatial distribution of lipofuscin, that is, no specific sets of cells have a greater specific accumulation of lipofuscin. A closer examination with a single optical slice (Figure 1Aii, bottom panel) revealed that lipofuscin is most easily detectable in the cell body rind (CBR; white dotted outline), which is a layer of cell bodies adjacent to the various neuropil regions. In contrast, autofluorescence is almost absent in the synapse/axon-rich neuropil. Lipofuscin accumulation in *spin* mutant brains was also verified with Sudan-Black-B (SBB; previously reported to label lipofuscin [Georgakopoulou *et al.*, 2013]). A general enhancement of SBB staining was observed in the brain of mutant flies (Supplemental Figure 2). It should be noted that SBB, even in control fly tissues, appears to additionally label lipid droplets in the fat bodies. For the remainder of this study, we have used autofluorescence in *spin* brain as an indicator of lipofuscin.

Lipofuscin is evident in brains as early as adult emergence (1 d) and becomes progressively more pronounced by 8 d of age. Thus, there is progressive accumulation of lipofuscin in *spin* mutants as compared with age-matched control brains. Our lipidomics analysis of single adult brains comprising ~100,000 cells (Ito *et al.*, 2013) enabled us to determine whether perturbations in major membrane lipids of the brain occur in conjunction with lipofuscin accumulation. In the course of this experiment, 41 membrane lipids belonging to six classes were quantified. PE, PC, and PE-ethers
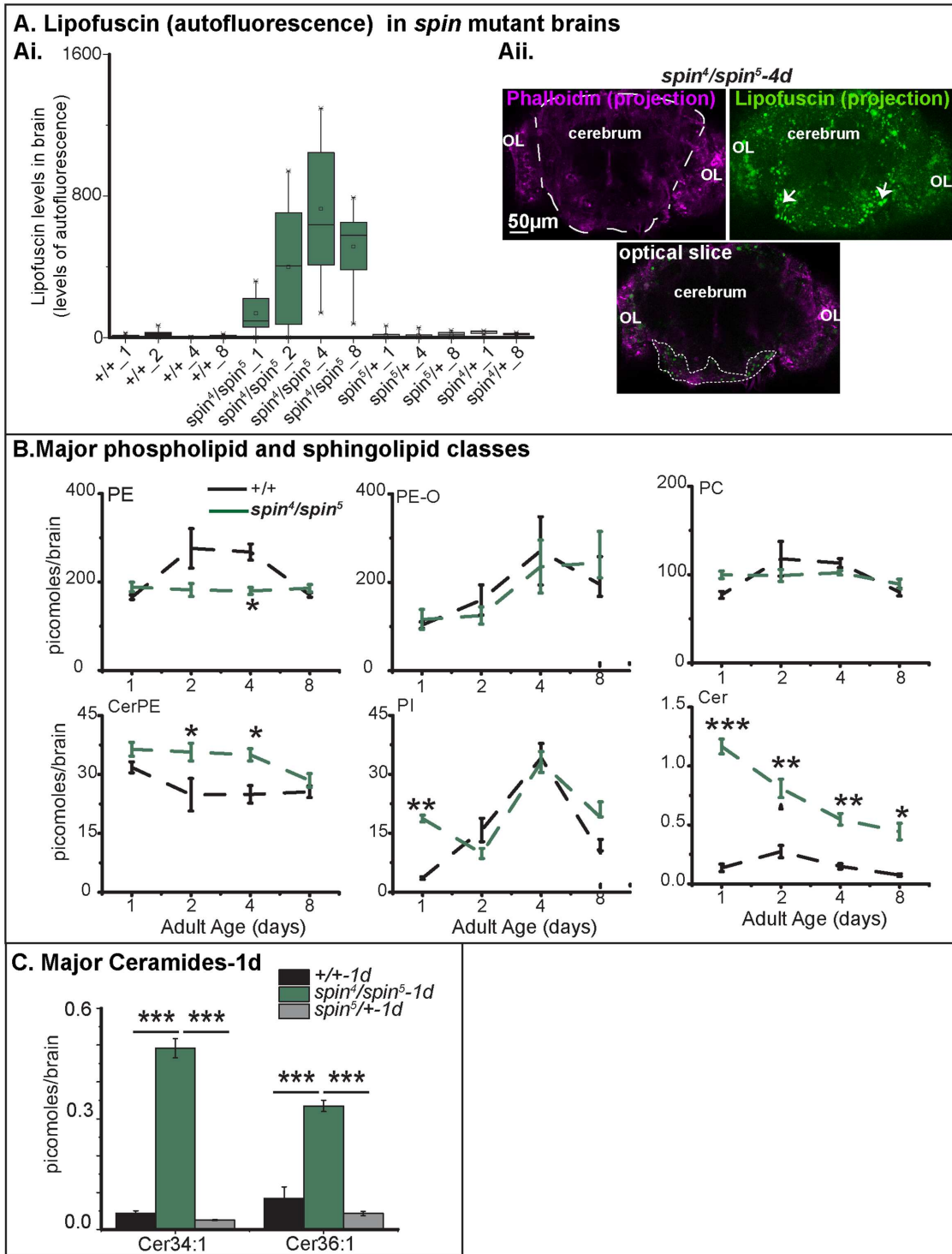
FIGURE 1: Lipofuscin accumulation and sphingolipid imbalance in *spin* mutant brains. (Ai) Box plot represents level of lipofuscin, indicated by autofluorescence, in dissected adult brains of *spin⁴/spin⁵* (green), genetic controls (*spin* heterozygotes, gray), and wild-type (+/+, black). Adult age in days is denoted after the genotype on the *x*-axis. The box ranges between 25th and 75th percentiles, whereas the whiskers denote the minimum and maximum values in the data set. Autofluorescence levels are variable, but it is evident that *spin⁴/spin⁵* (green) brains have much higher levels of autofluorescence than age-matched genetic controls (gray and light gray) or wild-type (black) brains. (Aii) Representative images of freshly dissected/nonpermeabilized adult *spin⁴/spin⁵* brains at 4 d of age stained with Alexa 555-phalloidin (magenta). Lipofuscin is visualized with autofluorescence (green). The top panel is a *Z*-stack visualized as a maximum intensity projection with the two channels separated out, and the bottom image is one optical slice with the two channels merged. The cerebrum (in the top panel) is demarcated with a white dashed line, and optic lobes (OL) are specified. Arrows (top panel) point to autofluorescent puncta, whereas the dotted white region (bottom image) denotes the CBR with autofluorescent puncta. Scale bar = 50 μm. (B) Values are mean ± SEM for lipid levels (quantified as

FIGURE 2: Abnormal accumulation of endomembranous structures. (A) Representative TEM images of cell bodies in the cortex of the adult brain at 2 d for *spin4/spin5*, *spin4/spin58*,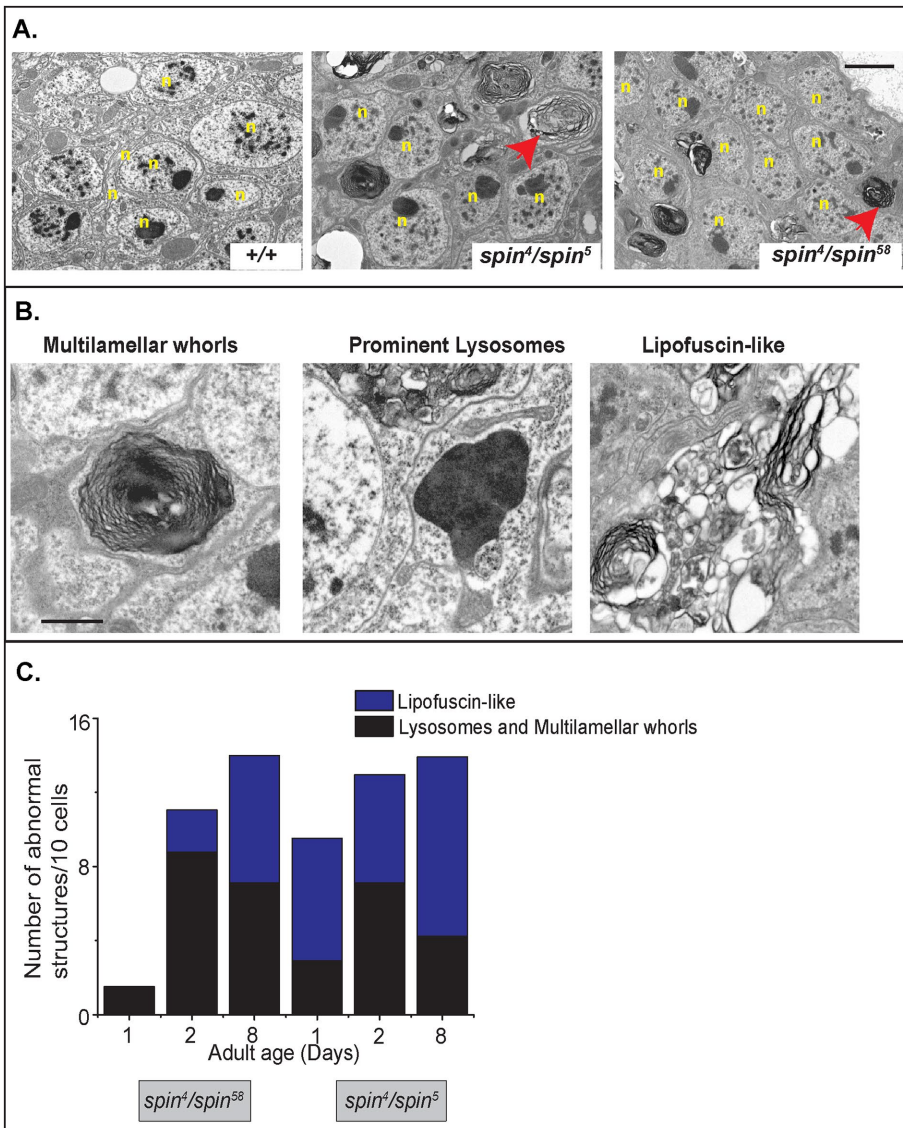 and wild-type (+/+). In both *spin* mutant heteroallelic combinations abnormal structures (red arrows) were observed. Nuclei of the cell bodies are indicated as *n*. Scale bar = 2 μm. (B) Representative images of different endomembranous structures observed in *spin* mutant brains: (i) lamellar whorls, (ii) electron dense lysosomes, and (iii) lipofuscin. Scale bar = 1 μm. (C) Occurrence of abnormal structures (lipofuscin, lamellar whorls, and prominent lysosomes) quantified as number of abnormal structures normalized to 10 cells (*n* = 3 animals) in *spin* mutant transheterozygotic (*spin4/spin5*, *spin4/spin58*) brains. In age-matched wild-type brain (1–8 d of adulthood), these abnormal structures are almost never observed.

Ceramides were the most prominently and consistently altered lipid class; an increase of more than 800% on day 1 in *spin* mutant brains (Figure 1B) as compared with controls was observed. This remarkable elevation in ceramide levels in *spin* brains was driven by increase in the major molecular species of ceramides, 32:1 and 34:1 (Figure 1C). It should be noted, however, that the magnitude of increase in ceramides in *spin* mutant brains is lowered on day 2 (more than 200%), day 4 (more than 350%), and day 8 (more than 590%) as compared with the initial surge on day 1. No change in ceramide levels was observed in *spin* mutant larval brains (Supplemental Figure 3). Because of partial lethality in the pupal stages (Nakano *et al.*, 2001; Sweeney and Davis, 2002; Dermaut *et al.*, 2005; Hindle *et al.*, 2011), it is difficult to pinpoint the exact onset of the ceramide imbalance. From our results, ceramide levels are increased at the onset of adulthood but could have been initiated during adult brain development in metamorphosis.

The other lipid classes, such as phosphatidylinostil (PI), PE, and CerPE, show significant increases but the difference is neither sustained nor indicative of any consistent trend on the subsequent days (Figure 1B). Because of the significant and overall increase in ceramide levels in *spin* brains at all the time points, the remainder of our analyses has focused on sphingolipids and the early onset change on day 1.

Occurrence of lipofuscin correlates with phenotypic severity of *spin* mutants

The occurrences of lamellated whorls and endomembranous structures are characteristic ultrastructural hallmarks of several degenerative diseases including LSD. Indeed, such structures have been previously reported in *spin* mutant retinas and in other fly models of LSD (Nakano *et al.*, 2001; Dermaut *et al.*, 2005; Hickey *et al.*, 2006). We therefore asked whether ultrastructural abnormalities in *spin* mutant brains coincide with altered lipid levels. Three categories of abnormal structures were observed in *spin* mutant brains that were not observed in age-matched control brains (Figure 2A); these include lamellated whorls/multi-lamellar whorls, prominent electron dense lysosomal structures, and a combination of dense bodies with

(PE-O) are the most abundant phospholipids and CerPE is the most prominent sphingolipid class in adult brains, which is similar to the larval brain lipidome (Carvalho *et al.*, 2010, 2012; Palm *et al.*, 2012; Ghosh *et al.*, 2013).

picomoles/brain) from single brains previously imaged for lipofuscin (top panel). Dotted lines are indicative of trends over the ages analyzed (1, 2, 4, and 8 d of age). Green indicates *spin4/spin5*, whereas black indicates wild-type (+/+). *$p < 0.005$, **$p < 0.00005$, ***$p < 0.00000005$ as indicated by post-hoc Tukey test following ANOVA. (C) Bar graphs represent absolute levels of major ceramide species (Cer34:1 and Cer36:1) on day 1 in brain extracts of *spin4/spin5* (green), genetic controls (*spin* heterozygotes, gray), and wild-type (+/+, black). Values are mean ± SEM quantified as picomoles/brain. ***$p < 0.00000005$ as indicated by post-hocTukey test following ANOVA.
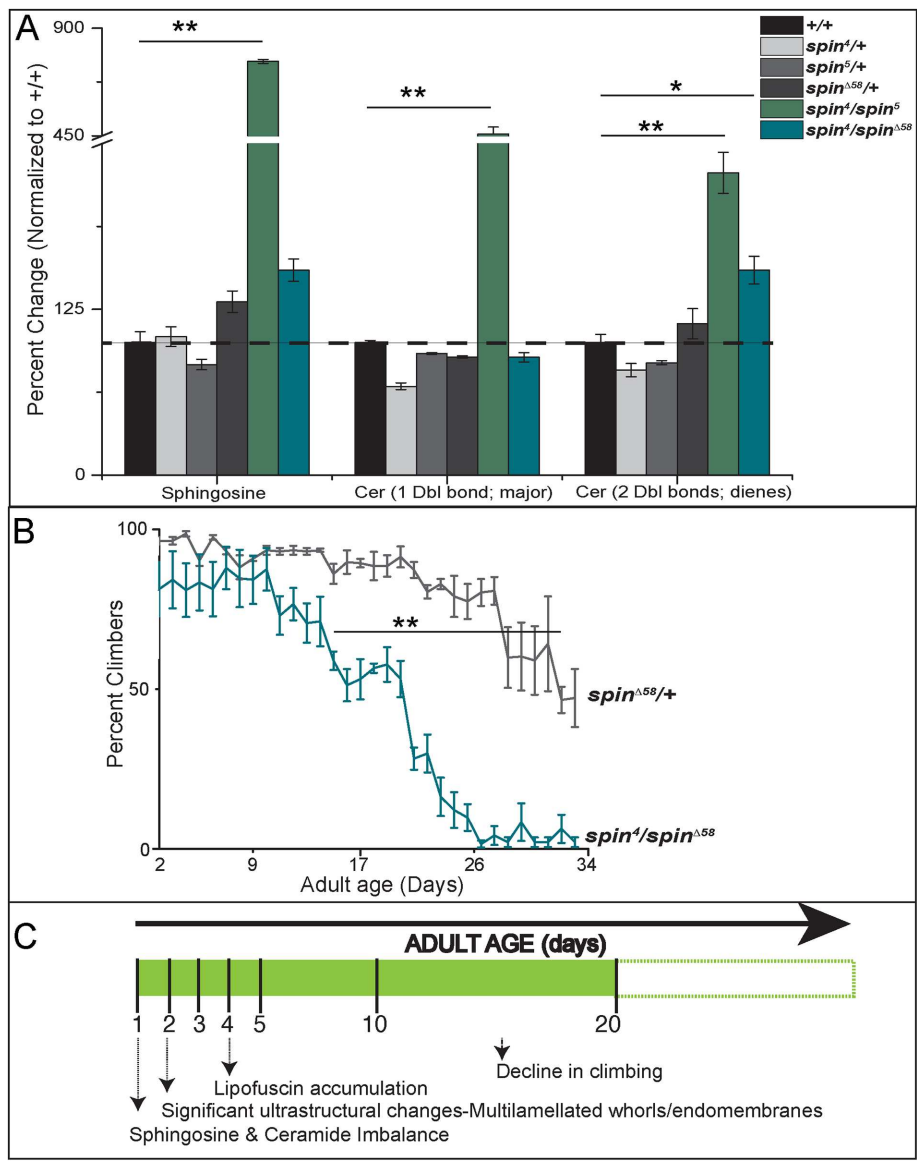
FIGURE 3: Ceramide/sphingosine imbalance occurs before behavior change. (A) Altered sphingosine/ceramide levels in two heteroallelic combinations of *spin* mutants. Bar graphs indicate percentage change in levels of sphingosine (Sph) and ceramides (one double bond or two double bonds; diene species) measured on day 1 of eclosion in adult brains compared with wild type. Values are mean± SEM, and *$p < 0.05$ and **$p < 0.01$ as calculated by post-hoc test following ANOVA. Black line indicates the baseline levels in control (+/+) to which all other lipid levels (picomoles/brain) are normalized. (B) Progressive loss of climbing behavior in *spin* mutant. Line graphs indicate trend of changing climbing behavior; each data point constitutes the daily average for percentage climbers ± SEM from three independent trials of 10–15 flies/trial over age (x-axis). **$0.001 < p < 0.05$, Student's *t* test. (C) Timeline relating ceramide and sphingosine imbalance during adult lifespan and the onset of specific neurodegenerative attributes such as lipofuscin accumulation and decline in climbing behavior in *spin* mutants.

lamellated whorls and membrane-bound structures (Figure 2B, left to right). The last category is reminiscent of lipofuscin—an outcome of increased oxidative stress and intracellular debris in degenerating and ageing cells. Lamellated whorls and prominent lysosomes were observed at a higher frequency at the onset (1–2 d of adulthood) as compared with 8 d, when lipofuscin-like structures become increasingly abundant (Figure 2C). These structures are also consistently observed in another allelic combination, *spin⁴/spin^Δ58*, that exhibit

a milder phenotype with regard to adult life span (Supplemental Figure 1). When we compared the two allelic combinations, the more severe *spin⁴/spin⁵* versus the milder *spin⁴/spin^Δ58*, we recognized that the stronger phenotype with reduced life span (Supplemental Figure 1) correlated with an earlier occurrence and a higher frequency of lipofuscin (Figure 2C). It should be noted that these abnormal structures were not observed in age-matched control brains at these early stages of the adult lifespan, that is, up to 8 d after eclosion. We conclude that because lamellar whorls precede the formation of lipofuscin, they constitute an earlier phenotype than lipofuscin in the disease progression.

Degree of ceramide and sphingosine elevation in adult *spin* brains correlates with the severity of neurodegeneration

The increase in ceramide levels, observed with single brains (Figure 1), was further confirmed when we measured ceramide and its low-abundance breakdown metabolite, sphingosine (Sph), using larger amounts of brain tissue. Consistent with single brain measurements, we observed a dramatic increase in ceramides on day 1 of adulthood (Figure 3A) in *spin⁴/spin⁵* mutants. For sphingosine, we observed a tremendous increase in abundance for *spin* mutants (Figure 3). We also note a smaller but significant increases in sphingosine and ceramide levels in the second heteroallelic combination *spin⁴/spin^Δ58* but to a lower extent (Figure 3). Here, statistically significant changes were only detected in ceramide dienes. Overall, the changes for *spin⁴/spin^Δ58* are less pronounced when compared with *spin⁴/spin⁵* brains but are consistent with the milder survival and ultrastructural phenotypes.

The enhanced viability of *spin⁴/spin^Δ58* heteroallelic combination over *spin⁴/spin⁵* enabled us to investigate the chronological coincidence of ultrastructural abnormalities, lipid alterations, and behavioral impairment. Here we used changes in the climbing ability of adult flies as a general indicator of behavioral alteration/impairment. Decreased climbing ability is displayed only after 2 wk of adult age (Figure 3B; see the Supplemental Movies). Our experiments suggest that ceramide and sphingosine metabolic perturbations constitute an early-onset event in these mutants, after which other signs of neurodegeneration such as ultrastructural abnormalities, lipofuscin accumulation, and behavioral impairment become pronounced (time line summarized in Figure 3C).

Ceramide imbalance is central to the role of *spin* in maintenance of adult neurons

To show that *spin* function is causally connected to perturbed ceramide/sphingosine levels, we carried out a genetic rescue
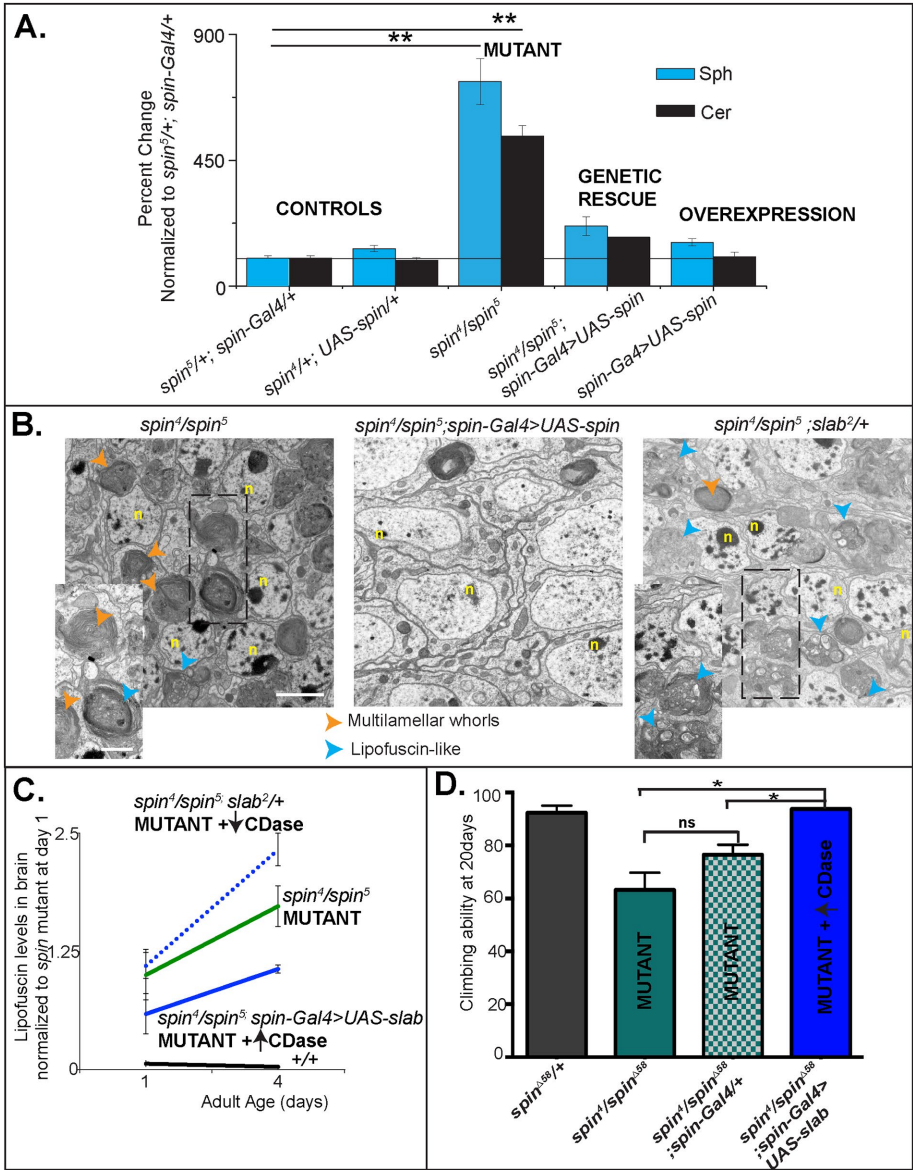
FIGURE 4: Rescue of $spin^4/spin^5$ phenotypes with *spin* overexpression and modification of $spin^4/$ $spin^5$ phenotypes with *slab (Ceramidase)* manipulation. (A) Bar graphs indicate percentage change in levels of sphingosine (blue bars) and total ceramides (black bars) measured on day 1 of eclosion in adult brains for mutant, genetic controls, rescue, and overexpression genotypes (also indicated along the *x*-axis). Lipid levels are quantified as picomoles of lipid/brain and percentage change with respect to genetic control ($spin^5/+; spinGal4/+$) are calculated, values are mean ± SEM, and **$p < 0.000001$ as calculated by post-hoc test following ANOVA. (B) Representative TEM images of cell bodies in the cortex of the adult brain at 4 d of $spin^4/spin^5$ (mutant), $spin^4/$ $spin^5; spin-Gal4>UAS-spin$ (genetic rescue) and $spin^4/spin^5; slab^2/+$ (mutant + decreased *Cdase*). In *spin* mutants alone and mutant + decreased *Cdase* combinations, abnormal structures (arrows) were observed. Insets show these abnormal structures at a higher magnification. In the case of the mutant alone, there are prominent lamellar whorls (orange) and a few lipofuscin-like strunctures (blue). These abnormal structures are strikingly absent on genetic rescue, but in the case of mutant + decreased *Cdase* combinations, there is an abundance of lipofuscin-like structures (blue). Nuclei of the cell bodies are indicated as *n*. Scale bar = 1.8 μm and 0.8 μm for insets. (C) Line profiles represent the mean ± SEM for normalized level of lipofuscin (indicated by autofluorescence) at 1 and 4 d of age in dissected adult brains of $spin^4/spin^5$ (green), wild-type (+/+,black), and on manipulation of *slab* (Cdase) in the background of *spin* mutants- $spin^4/spin^5;$ $slab^2/+$(blue dotted) and $spin^4/spin^5; spin-Gal4> UAS slab$ (blue). The levels are normalized to that of *spin* mutants on day 1 of eclosion. Lipofuscin levels steadily increase in *spin* mutants between day 1 and day 4. Introduction of *slab/+* in the *spin* background results in an even greater accumulation of lipofuscin whereas this trend is reversed with an overexpression of *slab* in the *spin* mutant background. (D) Graph represents climbing behavior at 20 d of age in adults for the genotypes indicated. Bars are mean ± SEM of percentage climbers. Mutants include $spin^4/spin^{\Delta58}$

experiment wherein full-length wild-type *spin* (isoform III) is overexpressed in the background of the mutant, $spin^4/spin^5$, specifically in cells where the endogenous *spin*-promoter is active (Sweeney and Davis, 2002). Lipid metabolic alterations are rescued by the transgene in this background. The abnormally high levels of brain ceramide and sphingosine in $spin^4/spin^5$ were reduced in rescued genotypes to levels almost comparable to the controls (Figure 4A). In the rescued genotypes, relative to the genetic controls, ceramide increase is only 74% as compared with 437% in the mutant, whereas sphingosine increase is only 61% as compared with 631% in mutants. The altered ceramide/sphingosine levels in the rescue genotypes also correlate with the life span of these animals; life span is longer in rescued animals than the mutant background but lower than in the controls (Supplemental Figure 1). Finally, the ultrastructural hallmark of *spin* mutant brains, which is the abundance of lamellar whorls, is significantly diminished on genetic rescue with *spin* overexpression (Figure 4B). Thus sphingolipid imbalance and the associated neurodegenerative attributes (reduced survival, progressively shortened life span, and ultrastructural abnormalities) described for *spin* mutants are all rescued by an overexpression of *spin*. These rescue experiments therefore underline that *spin* isoform III, as opposed to the other four isoforms (Nakano et al., 2001), is minimally sufficient to rescue most of the adult onset degeneration and related attributes in *spin* mutant flies. The residual effects on lifespan in these rescued genotypes could be explained due the lack of the other *spin* isoforms.

To test whether ceramide/sphingosine imbalance is causal to the degenerative attributes in *spin* brains, the *slab (ceramidase/Cdase)* (Rohrbough et al., 2004) gene was manipulated in the background of *spin* mutants. Mutants and overexpression lines of *slab* exhibit altered levels of ceramides as characterized by MS measurements (Acharya et al., 2003, 2008). *slab* heterozygotes and overexpression of *Cdase* specifically in neurons showed an increase and decrease of brain ceramides by more than 200 and 30%, respectively (Hebbar et al., 2015).

(teal colored bar) and the same heteroallelic combination with spin-Gal4 in the background $spin^4/spin^{\Delta58}; spin-Gal4/+$ (teal and grey colored bar). Overexpression of *slab* in this background resulted in a rescue of the climbing behavior (blue bar for $spin^4/spin^{\Delta58};$ $spin-Gal4>UAS slab$). *$p < 0.05$ for each pair when compared with Student's *t* test.

Therefore, these genetic tools were combined in the background of *spin* mutants. Ultrastructural defects as well as lipofuscin accumulation were used to score the extent of the degenerative phenotype against *spin* mutant alone. Reducing *slab* levels (with *slab²* heterozygosity; *slab²/+)* in the background of *spin* mutant, and consequently further pushing ceramide levels higher (documented for *slab²/+* in Hebbar *et al.*, 2015), correlated with an intensification of these degenerative phenotypes. This effect is most clearly evidenced (at day 4 of adulthood) by the increased presence of ultrastructural defects (Figure 4B) and enhanced autofluorescence by 34% (Figure 4C) in *spin⁴/spin⁵; slab²/+*. The abundance of lipofuscin-like structures as opposed to lamellar whorls in age-matched *spin⁴/spin⁵; slab²/+* neurons (Figure 4B) highlights the severity and progression of degeneration caused by a reduction of *slab* function (and increase in ceramides) in *spin⁴/spin⁵* brains. In contrast, overexpression of *slab*, and consequently reducing ceramide levels (documented in Hebbar *et al.*, 2015), halted the formation and accumulation of lipofuscin with age (Figure 4C). A 42% reduction in lipofuscin levels was seen at the onset (day 1) and a 39% reduction was observed at a later stage (day 4) in *spin⁴/spin⁵; spin-Gal4>UAS slab* as compared with *spin⁴/spin⁵*. Further this interaction between *spin* and *slab* also extends to the phenotype of behavioral decline observed in *spin* mutants. Using a different allelic combination (*spin⁴/spin^{Δ58}*) that permits quantification of climbing behavior, we compared climbing behavior in *spin* mutants (*spin⁴/spin^{Δ58}*) alone and with overexpression of *slab* (*spin⁴/spin^{Δ58}; spin-Gal4>UAS slab)*. On overexpression of *slab* in the *spin* mutant background, we observed that the reduced ability of *spin* mutants to climb is rescued (Supplemental Figure 4). By 20 d of adulthood, whereas *spin* mutants have ~30% reduced climbing ability, the overexpression of *slab* in *spin* mutants improved climbing ability to that seen in controls (Figure 4D).

This epistatic relationship between ceramide manipulation and *spin* mutant abnormalities suggests that lowered ceramide levels in *spin* brains correspond to lowered accumulation of lipofuscin and behavioral decline. However, it should be noted that *slab* manipulation did not correlate with developmental lethality/viability of *spin⁴/spin⁵*; we observed that *slab* overexpression or *slab²/+* in the *spin⁴/spin⁵* background caused increases in *spin⁴/spin⁵* viability (of 7 and 20%, respectively) to adulthood. This finding probably indicates that the genetic interaction of *slab* and *spin* is not critical during development but becomes important during adulthood.

The *spin* rescue experiments and the genetic interaction with *slab* help delineate that the removal of *spin* function in *Drosophila* causes an early-onset imbalance in sphingolipid metabolism during adulthood. Elevated levels of ceramides and sphingosine are responsible for the progression of the disease leading to a loss of neuronal health and to changes in behavior. It remains unclear if these lipids are specifically enriched in the observed ultrastructural abnormalities.

Interactors for Spin have roles in carbohydrate and lipid metabolism

In an effort to identify intracellular processes impaired by loss of function of *spin*, we sought to determine its direct protein interactors by coimmunoprecipitation and proteomics (see Supplemental Figure 5 for details). In this way, 29 interactors for Spin were detected and are summarized in Table 1. Using the PANTHER Classification System (Thomas *et al.*, 2003; Mi *et al.*, 2005), these proteins were classified according to their listed cellular component ontology. Thirteen proteins localize to the mitochondrion and are involved in glycolysis. Glycolytic enzymes are recruited to the syn-

apses during energy demand (Jang *et al.*, 2016). Since Spin is actively trafficked along axons (Kumarasamy *et al.*, 2008; Lim and Kraut, 2009) via an energy demanding process, these proteins constitute a potentially intriguing cluster. Further, one protein (guanine nucleotide-binding protein subunit beta-like protein/Rack1) is assigned to the endosome, whereas the lipoprotein (Apolipophorin; ApoLpp) is assigned to the autophagosome; both of these subcellular locations are relevant given the previously published information on Spin localization to the late endosome/lysosome (Sweeney and Davis, 2002; Lim and Kraut, 2009; Rong *et al.*, 2011). In the context of a multi-organ and systemic lipid metabolic imbalance in LSD, we focused on the relevance of Lpp (the functional lipoprotein produced from ApoLpp) as a direct interactor of Spin. Lpp constitutes the lipid transport protein in *Drosophila* that originates in the fat bodies and facilitates interorgan lipid movement, including the delivery of lipids (Brankatschk and Eaton, 2010; Palm *et al.*, 2012). To confirm the interaction between Lpp and Spin, we investigated Lpp and Spin localization in tissues throughout the body. In the adult brain, Spin-GFP driven by *spin-Gal4* is seen in the neuropil and cortex. In the cortical areas, punctate staining for Spin is evident and a subset of these structures are positive for Lpp immunoreactivity (Figure 5, A and A″). We further observed colocalization in fat bodies, where both Spin-GFP and Lpp (Brankatschk and Eaton, 2010) are also abundantly present (Figure 5B). Consistent with neuronal staining, a subset of Spin and Lpp are colocalized in compartments that are in close proximity to the membrane (Figure 5B′).

In *spin* mutant adult brains, we observed a change in Lpp staining as compared with the rescue genotypes (Figure 6A). To better identify the nature of this change, 10-μm sections were imaged (Figure 6B) instead of the whole brain (Figure 6A). Focusing on the CBR, with neuronal nuclei marked with an antibody to elav, Lpp puncta are observed in the brains (Figure 6, B and B′). However, fewer Lpp-containing punctate structures are observed in mutant brains (Figure 6B″). Lowered Lpp staining in mutants was also consistently observed in other tissues; one such example includes the oenocytes. These cells are labeled very strongly when Spin-GFP is driven using *spin-Gal4* indicative of *spin* expression (Figure 5C). Adult oenocytes are a band of cells present dorsally and ventrally along the abdominal cuticle (Figure 6, B and C, and Supplemental Figure 6; Billeter *et al.* (2009). Oenocytes regulate lipid metabolism and energy storage (Gutierrez *et al.*, 2007), making them an ideal tissue to gain further functional insight into the Spin–Lpp connection. Adult oenocytes act as centers for the production of cuticular hydrocarbons, several of which function as pheromones (Billeter *et al.*, 2009; Yew and Chung, 2015). Since cuticular hydrocarbons (CHCs) are synthesized by the extension and modification of fatty acid precursors (Yew and Chung, 2015), we hypothesize that Spin-LPP will influence CHC synthesis in the oenocytes. Support for this hypothesis comes from two observations. First, Lpp immunostaining in *spin* mutant oenocytes (Figure 6E) is altered, with a reduced intensity (as compared with rescue conditions [Figure 6C′] and wild-type conditions [Figure 6D]; see more examples in Supplemental Figure 6). Second, total amounts of CHCs are significantly increased in *spin* mutant females (Figure 6F) while there is no change in specific CHC content. Taken together, these observations point to an intriguing possibility that Spin–Lpp interaction plays a role in regulating CHC synthesis. Whether it is the delivery of the fatty acid precursors to the oenocytes, the actual biosynthesis, or the subsequent transport of the CHC from the oenocytes remains to be addressed. Moreover, whether there are general deficits in lipid metabolism, interorgan lipid transport, or Lpp production/transport are interesting questions for future research.

No.	Peptide ID (Uniprot)	Protein name	Associated fly gene ID
1	Q01604	Phosphoglycerate kinase	CG3127
2	Q9VEB1	Malate dehydrogenase2	CG7998
3	P15007	Enolase	CG17654
4	Q0E9E2	Pyruvate carboxylase	CG1516
5	B7Z0E0	Isocitrate dehydrogenase (NADP)	CG7176
6	Q9W4H6	GM13002p/pyruvate dehydrogenase	CG7010
7	Q7KVX1	Lethal (1) G0334, isoform C/pyruvate dehydrogenase	CG7010
8	Q7K5K3	GH08474p/ pyruvate dehydrogenase (acetyl-transferring) activity	CG11876
9	P41572	6-Phosphogluconate dehydrogenase	CG3724
10	P52029	Glucose-6-phosphate isomerase	CG8251
11	P52034	6-Phosphofructokinase	CG6001
12	Q9VHN7	CG8036, isoform B/transketolase	CG8036
13	Q9V496	Apolipophorin	CG11064
14	P11997	Larval serum protein 1 gamma chain	CG6821
15	O18404	3-Hydroxyacyl-CoA dehydrogenase type-2	CG7113
16	Q9VSA3	Probable medium-chain specific acyl-CoA dehydrogenase, mitochondrial	CG12262
17	P02844	Vitellogenin-2	CG2979
18	Q94511	NADH-ubiquinone oxidoreductase, 75kDa subunit	CG2286
19	Q7KN94	Walrus, isoform A/FAD binding	CG8996
20	Q95U46	GH07925p/flavin adenine dinucleotide binding	CG3902
21	Q95U38	GH10480p/succinate-CoA ligase (ADP-forming) activity	CG11963
22	Q9VNW6	GH12632p/Glutamate 5-kinase	CG7470
23	Q9VYD9	AT04676p/L-alanine:2-oxoglutarate aminotransferase activity	CG1640
24	Q9VLC5	Aldehyde dehydrogenase	CG3752
25	P54399	Protein disulfide-isomerase	CG6988
26	Q9VC18	CG11089/IMP cyclohydrolase activity	G11089
27	Q9VFC7	Myofilin, isoform B/Mf5	CG6803
28	A1ZA66	Stretchin-Mlck, isoform A	CG18255
29	O18640	Guanine nucleotide-binding protein subunit beta-like protein/Rack1	CG7111

TABLE 1: Identified Spin interactors.

DISCUSSION

We identified alterations in brain ceramide and sphingosine levels in adults following loss of *spin* function. Perturbations in lipid quantities occur prior to the onset of endomembrane accumulation and before the functional and morphological attributes of neurodegeneration are evident (summarized in Figure 3C). These observations are comparable with reported elevation in sphingosine in cell lines on drug induction of LSD (Lloyd-Evans *et al.*, 2008). Recent studies have linked oxidative stress, lipid droplet formation, neutral lipid storage, and neuronal health in *Drosophila* and mice tissues (Liu *et al.*, 2015). Our approach has enabled us to define the nature and dynamics of these lipid perturbations and confirm the suspected links of lipid imbalance and pathological attributes of degeneration in a temporal and tissue-specific manner.

We argue that this loss of ceramide/sphingosine homeostasis is not due to apoptosis but is directly linked to loss of *spin* function. An indication that enhanced apoptosis is not the underlying cause is evident from the absence of any notable apoptotic-like features (vacuolization) in the transmission electron microscopy (TEM) im-

ages of 1-d-old brains (Figure 2). That *spin* function is causally connected to ceramide and sphingosine is further validated by our rescue experiments.

The *slab/Cdase* and *spin* interaction experiments clearly establish loss of *spin* function upstream of the ceramide imbalance. The altered sphingolipid level is responsible for behavioral decline and lipofuscin accumulation. Given the chronology of events (summarized in Figure 3C) and the outcome of our genetic interaction/rescue experiments, it is evident that accelerated lipofuscin accumulation, as a result of perturbed ceramide levels, correlates with the loss of nervous system integrity in *spin* mutants. How does the loss of Spin result in a perturbation of sphingolipids? There is no evidence from our study, or elsewhere, to suggest a direct role for *spin* in ceramide or sphingosine biosynthesis. However, Spin is assumed to function as a sphingosine-1-phosphate transporter (Osborne *et al.*, 2008; Kawahara *et al.*, 2009). Since our measurements are limited snapshots of the brain lipidome, we cannot make any speculations on the dynamics of ceramide/sphingosine and S1P transport in relation to *spin* function.
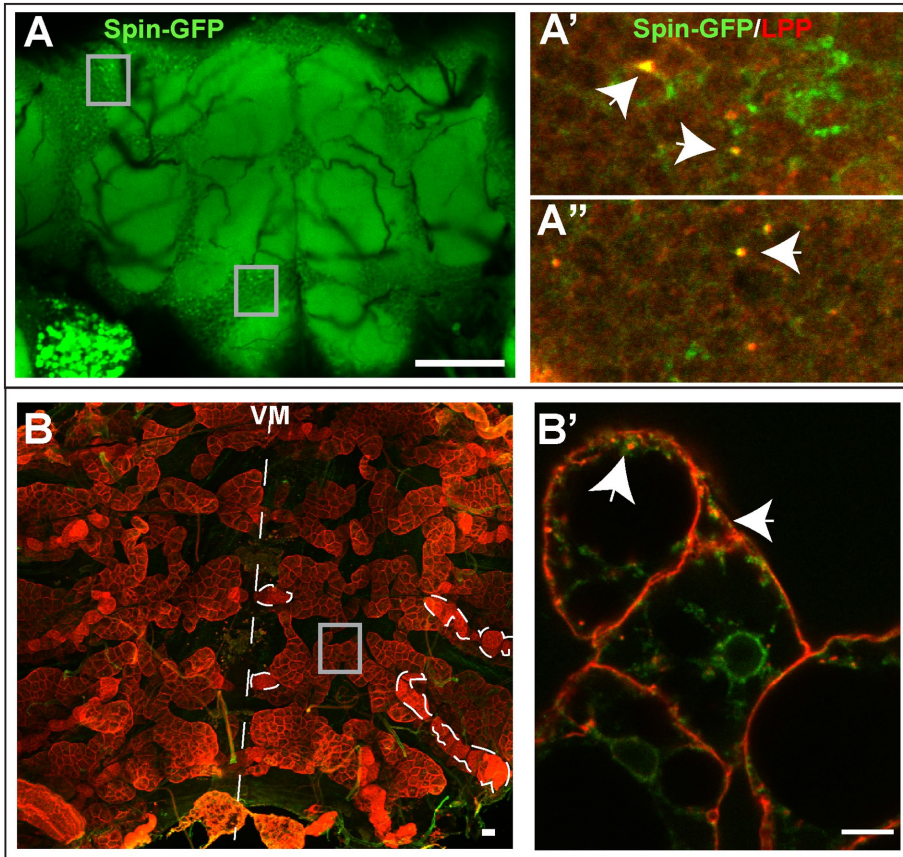
FIGURE 5: Spin–Lpp interaction. A–B': Representative images of (A–A") adult brain and (B–B') adult abdomen of *spin-Gal4>Spin-GFP* animals labeled with GFP (green) and Lpp (red) antibodies. Scale bar = 50 μm. In the abdominal fillet preparation, ventral midline is indicated with a dashed white line and fat bodies (gray box) and oenocytes (dashed outline) display LPP staining. Boxed regions are imaged at high magnification and shown in A', A", and B'. Arrowheads indicate subset of Spin-GFP-positive puncta that also display LPP immunoreactivity in neuronal cortex (above) and in fat bodies (below). Scale bar: 10 μm.

It is possible that the loss of Spin causes an altered partitioning of sphingosine in the late endosomal/lysosomal compartments, which leads to aberrant signaling. It has been recently shown that sphingosine in cultured cells has the potential to release calcium from acidic compartments, which in turn can influence autophagy, relevant for the turnover of proteins and lipids (Hoglinger *et al.*, 2015). A second likely possibility stems from observations that loss of Spin results in the incomplete progression of autolysosomal reformation and the accumulation of autolysosomes (Rong *et al.*, 2011). We hypothesize that altered *spin* function in adult neurons accelerates or enhances the formation of autophagic structures such as autolysosomes. This disruption leads to a failure to completely recycle components, including lipids such as ceramides and sphingosine. Since the process is most likely stalled, and further exacerbated by the elevated levels of these signaling lipids, there is an eventual accumulation of intracellular debris in the form of lipofuscin. In motorneuron degeneration of *bchs* mutants, a late endosomal protein, perturbations in autophagic flux cause the accumulation of these signaling lipids in autophagosomes, and this prevents prosurvival signaling involving mitogen-activated protein kinase (MAPK) and protein kinase B (Akt) (Hebbar *et al.*, 2015). Here, our electron microscopy data effectively demonstrate that changing levels of ceramide has consequences on disease progression by causing a detrimental ac-

cumulation of lipofuscin in *spin* mutants. Thus, in a manner similar to *bchs* larval motorneuron degeneration, an overlap between perturbations in ceramide/sphingosine signaling and *spin* function in autophagy could underlie the age-associated degeneration of adult *spin* mutants. Since all these three processes, namely a lipid metabolic imbalance, neurodegeneration, and autophagy, are implicated in LSD (Hoglinger *et al.*, 2015), this work extends our understanding of the sequence of events in this disease model. Some relevant aspects of the above model are, however, unresolved. First, the relative contribution of elevated ceramides and sphingosine in maintaining integrity in the brain is unknown. This is difficult to resolve because their metabolic pathways are interconnected. However, it will be relevant to elucidate the nature of ceramide/sphingosine downstream signaling that causes the aberrant progression of autophagy and leads to the formation of lipofuscin. Second, it will be important to also address if an imbalance of ceramides/sphingosine is only limited to signaling within, or from, lysosomal/autophagic structures. Indeed, our experiments with *slab* and *spin* suggest that changing overall levels, presumably in all membranes, certainly has an impact. Recently photoactivatable "caged" sphingosine was used to create elevated intracellular levels and its role in calcium signaling from the lysosome was demonstrated in cultured cells (Hoglinger *et al.*, 2015). It will be important in the future to employ such approaches to enable manipulation of these lipids in specific subcellular compartments and monitor the consequences on disease progression.

Interestingly in the mutants, although ceramide levels are consistently higher than the controls, the initial dramatic surge is lowered by 8 d of age. In the context of a storage disease, it will be interesting to evaluate the general metabolic outcome of imbalances in ceramide and sphingosine in *spin* mutants. Given the relevance of glycosphingolipids in the pathology of LSDs (te Vruchte *et al.*, 2004), it is crucial to ask whether the increased ceramide/sphingosine levels in *spin* mutants lead to the storage of complex glycolipids. Further, do the increased ceramides and sphingosine overlap with the increased oxidative stress? Indeed, *spin* mutant adult brains at 5 d posteclosion (Milton *et al.*, 2011) exhibit increased oxidative stress signaling. We propose that elevated ceramide levels in *spin* brains could potentially influence pathways that lead to the generation of reactive oxygen species (ROS), as demonstrated in a mouse model for perturbed ceramide synthesis (Zigdon *et al.*, 2013).

We have also identified potential metabolic and cellular interaction partners of Spin, including an interaction with Lpp and an impact of decreased *spin* function on Lpp levels in neurons and oenocytes. Our observations point to the likelihood that Spin and Lpp interact in the brain and also in adult oenocytic function, specifically in the overall production/transport of
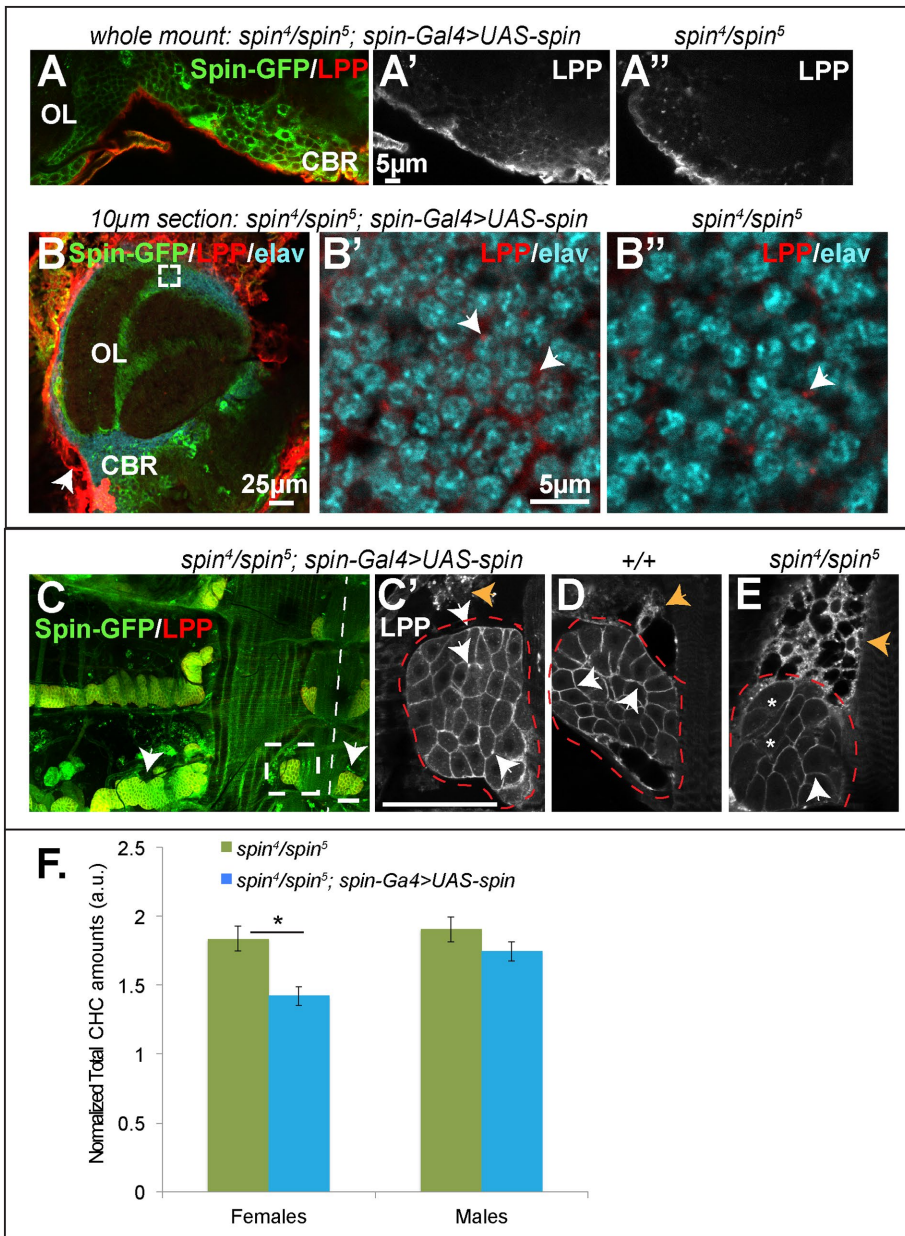
FIGURE 6: Decreased Lpp staining in *spin* mutants. (A, B) Labeling of Lpp in *spin* mutant and rescue neurons. (A) An optical section from a confocal *Z*-stack of dissected adult brain of *spin* rescue genotype (A, A′; *spin⁴/spin⁵; spin-Gal4>UAS-spin*) and mutant (A″; *spin⁴/spin⁵*). Tissues are immunostained with anti-GFP (Spin-GFP; green) and anti-Lpp (red). In the rescued genotype, the Spin-GFP (green) label is clearly visible in with the optic lobe (OL) and the cell body rind (CBR) of the adjacent neuropil in the cerebrum. Anti-Lpp immunostaining is shown separately in A′ and A″. Scale bar = 25 μm. (B) An optical section from a confocal *Z*-stack of a 10-μm adult head section of *spin* rescue genotype (B, B′; *spin⁴/spin⁵; spin-Gal4>UAS-spin*) and mutant (B″; *spin⁴/spin⁵*) immunostained with anti-GFP (Spin-GFP; green), anti-Lpp (red), and anti-elav (neuronal nuclei; cyan). The OL and associated CBR is visible in B. A higher magnification view of the CBR with neuronal nuclei (cyan) and anti-LPP (red) is shown in rescue (*spin⁴/spin⁵; spin-Gal4>UAS-spin*) and mutant (*spin⁴/spin⁵*). Lpp (red; indicated by white arrows) is decreased in the mutant. Scale bar = 25 μm (B) and 5 μm (B′, B″). (C–E) Labeling of Lpp in *spin* mutant and rescue oenocytes. Female adult abdominal fillet labeled with GFP and Lpp antibodies in (*spin⁴/spin⁵; spin-Gal4>UAS-spin*) rescued genotype. Rescue construct (Spin-GFP; green in C) is clearly evident in dorsal and ventral oenocytes (arrows in C); Ventral midline is indicated by white dashed line. Scale bar = 50 μm. Lpp distribution in ventral oenocytes (red outline) and adjoining fat bodies (orange arrow) is shown at a higher magnification (C′–E) in rescue (C′; *spin⁴/spin5; spin-Gal4>UAS-spin*), wild-type (D; *+/+*) and in mutant (E; *spin⁴/spin⁵*) genotypes. Lpp is visible at the membrane of oenocytic cells (white arrows), but the intensity of Lpp staining is reduced in *spin* mutants (E); there are some clusters of cells (white asterisk) wherein the membrane staining of Lpp appears diminished. Scale bar = 50 μm. (F) CHC quantification: Bars represent mean ± SEM for total cuticular hydrocarbon (CHC) levels in male and female flies from mutant (*spin⁴/spin⁵*) and (*spin⁴/spin5; spin-Gal4>UAS-spin*) rescued genotypes. Mutant females display significantly ($p < 0.05$) higher levels of CHCs as compared with rescued genotypes; $p = 0.01$, post-hoc Holm-Sidak test following ANOVA; $n = 3$ replicates of six to eight flies each.

CHCs. It also raises the hypothesis that Spin/Lpp interaction may be relevant in interorgan lipid transport and could have implications in systemic diseases such as LSD where multiple organs are affected. In conclusion, studying the contribution of these interacting proteins and the organs will throw light on the increasingly acknowledged connections among lipid metabolic imbalance, loss of cellular integrity, and the manifestation of disease pathology.

MATERIALS AND METHODS

Flies

All fly lines and genotypes used are listed in the Supplemental Material; see Supplemental Table 1. Flies were raised at 25°C on a regular yeast-sugar-cornmeal medium supplemented with fungicidal mixture of phosphoric acid and propionic acid (http://flystocks.bio.indiana.edu/Fly_Work/media-recipes/caltechfood.htm).

Lipofuscin imaging and analyses

Adult brains were dissected in phosphate-buffered saline (PBS) on ice. They were placed in Alexa568-labeled phalloidin (1:40; Life Technologies, India) for 20 min on ice before transferring onto PBS on glass slides for imaging. Brains were imaged using Fluoview 1000 (Olympus Corporation, Japan) with an Argon 488 (autofluorescence) and HeNe (568 phalloidin) laser. Optical sections were taken and merged using ImageJ (Schneider *et al.*, 2012) to create an image stack. Image stack was analyzed to give particle count to indicate number of fluorescent particles.

Immunostaining

Dissected adult brains and abdominal fillets were immunostained following Hebbar *et al.* (2006). The primary antibodies used were anti-GFP (A-11122, 1:200; Life Technologies, India), anti-elav (7E8A10, DSHB, University of Iowa, USA), and anti-Lpp (guinea pig, gift from Marko Brankatschk [Brankatschk and Eaton, 2010]). Fluor-tagged secondaries were obtained from Life Technologies, India.

Transmission electron microscopy

Adult heads were dissected, placed in fixative (4% paraformaldehyde, 1% glutaraldehyde in 0.1 M sodium phosphate buffer, pH 7.4), and vacuum treated to removed adherent air. Heads were incubated in fresh fixative overnight at 4°C. All incubations were on a rotating wheel, unless otherwise stated. Heads were washed in 0.1 M sodium phosphate buffer (3 × 10 min), postfixed in 1% OsO_4 for 1 h, followed by washes in 0.1 M sodium phosphate buffer (3 × 10 min), and dH_2O (3 × 10 min). Heads were dehydrated in an acetone series (30%, 50%, 70%, 90%, 3 × 100%; 20 min each) and then incubated in increasing concentrations of Spurr's resin:acetone (25%, 50%, 75%, 95%, 2 × 100% [at 37°C]; 45 min each) followed by incubation in 100% resin overnight at 4°C without rotation. Heads were embedded in Spurr's resin for 24 h at 70°C.

After reaching the desired depth by semi-thick sectioning, ultrathin sections (60–70 nm) were collected coated grids, treated with uranyl acetate in 50% ethanol (10 min), and submerged in dH_2O to wash. Sections were stained with lead citrate (10 min) in the presence of sodium hydroxide pellets, followed by washing in dH_2O. Images were acquired using analysis software on a TECNAI G^2 (Version 2.18) transmission electron microscope (120 kV).

SBB staining

Fly heads were dissected and fixed in 4% formaldehyde, embedded in tissue freezing medium, and cryosectioned at 10-μm thickness. SBB staining was performed as described in Georgakopoulou et al. (2013). Briefly, sections were rinsed in PBS (pH = 7.5). They were sequentially dehydrated in 50% and then 70% ethanol before immersing in SBB (0.7% in 70% ethanol) briefly. Excess stain was drained and sections prepared for microscopy.

Lipid extraction and lipidomics

Lipid extraction. Female adults of the required genotypes were collected on emergence and aged appropriately. Depending on the experiment, single brains or groups of three brains were dissected in PBS and flash frozen in liquid nitrogen and stored in 20% methanol to avoid any enzymatic degradation. Brain samples were homogenized and extracted according to the methyl-tert-butyl ether extraction method (Matyash et al., 2008). All lipid standards were added to the homogenates prior extraction (Supplemental Table 2). The upper methyl tert-butyl ether (MTBE) layer was dried and stored until measurement at –80°C. For the mass spectrometric measurements, the samples were dissolved in 100 μl methanol containing 0.1% ammonium acetate.

Lipidomics of single brains. To study the correlation between lipfuscin accumulation and lipid metabolism (Figure 1), single brains were homogenized directly after imaging and extracted with the MTBE based extraction protocol. LC-MS was performed on a Agilent 1200 microLC system (Agilent Technologies, USA) coupled with a LTQ Orbitrap XL mass spectrometer (Thermo Fisher Scientific, Bremen, Germany) using a split flow setup to perform nano-ESI with the Nanomate TriVersa (Advion BioSciences Ltd, USA). Liquid chromatography was performed at a flow rate of 20 μl/min using a Zorbax SB-C18 column (0.5 mm ID, 5 μm, 150 mm), and 5-μl samples were injected. Solvent A was methanol containing 0.1% ammonium acetate and solvent B MTBE. The gradient was as follows: 0–3 min, B = 0.5%; 18–21 min, B = 50%; and 22–37, min B = 0.5%. Extracted ion chromatograms for designated lipids were integrated using accurate masses (±5 ppm) with Xcalibur software (Thermo Fisher Scientific, Germany)

MS^n analysis of pooled brain lipid extracts. Lipid extracts were analyzed with a flow-injection system using a flowrate of 1 μl/min and 5 μl sample injection. Negative and positive ion mode spectra were acquired with a LTQ-Orbitrap XL equipped with a 1200 microLC system and a Nanomate Triversa utilizing 5-μm ID ESI-chips. In the negative mode, PI, PE, PE-O, lysophosphatidylethanolamine (LPE), PC, CerPE, phosphatidylserine (PS), and phosphatidylglycerol (PG) were identified according to their accurate mass as described earlier (Schwudke et al., 2011). For PS, the specific neutral loss of 87 Da was monitored in the linear ion trap and used for quantification. In the positive ion mode Sph 14:1, ceramides and hex-ceramides were monitored with MS^3 in the linear ion trap using the long chain base-related fragment ions. All MS^3 for quantifying sphingolipids were analyzed using Xcalibur software while all other analyses were performed using LipidXplorer (Herzog et al., 2011).

For single and pooled brains, absolute levels of individual lipid species were summed up to arrive at lipid class quantities. At least five biological replicates were used for the analyses. GraphPad Prism (GraphPad Software, USA) and Origin 8.1 (OriginLab, USA) were used to for graphical representation and Origin 8.1 for analysis of variance (ANOVA) coupled with post-hoc Tukey test.

Annotation of lipids. Phospholipids were indicated as ⟨lipidclass⟩ ⟨no. of carbons in all fatty acids⟩:⟨no. of double bonds in all fatty acids⟩. For the annotation of phosphatidyl ethanolamine vinyl ether and alkyl ether, the abbreviation PE-O was used along with the number of double bonds of the fatty acid and fatty alcohol moiety. Sphingolipids were annotated as ⟨lipid class⟩ ⟨no. of carbons in the long-chain base and fatty acid moieties⟩:⟨no. of double bonds in the long-chain base and fatty acid moieties⟩. Lipid class abbreviations were utilized and defined throughout the article.

Coimmunoprecipitation and proteomics analyses

Spin-GFP protein was pulled down, and interaction partners identified using a proteomics-MS approach; see the Supplemental Material for schematic on workflow. Briefly, using the Gal4-UAS system, we overexpressed Spin-GFP under the control of the endogenous *spin* promoter (*spin*-Gal4; Sweeney and Davis, 2002). As a control, we also used flies that had GFP being overexpressed with *spin*-Gal4. Using lysates from whole organisms, we immunoprecipated GFP using anti-GFP as the bait (GFP-Trap_A kit; Chromotek, Germany). The coimmunoprecipitated fractions were run on SDS–PAGE and each lane was cut into 10 slices, followed by in-gel digestion (Shevchenko et al., 2006). For each lane, slices were analyzed using 1200 nano-LC coupled to LTQ Orbitrap Discovery (Thermo Fisher Scientific, Germany) using Nanomate Triversa as ionsource. Peptide identification and protein assignments were performed using Protein Discoverer 1.3. (Thermo Fisher Scientific, Germany) and Mascot as a search engine. Only proteins with a minimum of two unique peptides and false discovery rate better than 0.01 were accepted as positive hits. Proteins specific to Spin-GFP co-IP fraction and not found in the control-GFP co-IP fraction were compiled from three independent experiments.

Climbing assays

Standard fly climbing assays were conducted to assay the climbing behavior in *spin* and control flies. For this, male and female flies were collected within 6 h of eclosion and separately maintained in groups of 10–20 flies with transfers into fresh food every 2–3 d. At 3 d of age, these flies were subjected to a climbing assay and subsequently assayed for the next 30 d. The climbing assay was conducted in a double-blind procedure (for the entire procedure until the data analysis was completed) in a room devoid of any obvious olfactory and visual

cues and temperature was monitored and maintained at 25°C. Briefly, flies were transferred to a glass vial with an "8 cm" mark on it. After acclimatization, the assay was video recorded starting with the tapping of the vial. Climbers were defined as flies that reached a height of 8 cm within 18 s. The assay was repeated three times and averages for percentage climbers was calculated from video recordings from a set of three independent vials/repeats with 10–20 flies each.

Life-span analyses

Adult males and females of relevant genotypes were separately collected within 6 h of emergence and kept in groups of 15–20. Flies were transferred into fresh food vials every 2 d, and the total number of surviving flies was recorded. These observations were used to calculate life-span curves and 50% survivorship (T-50), which is the length in days at which 50% of the flies remained alive (Fergestad et al., 2008).

CHC extraction and analyses

Samples for were prepared by incubating five to eight of each genotype at room temperature for 20 min with 120 µl of hexane containing 10 µg/ml hexacosane as an internal standard. The extract (100 µl) was transferred into a fresh glass vial and allowed to evaporate at room temperature. Samples were stored at –20°C. Three replicates were prepared for each genotype.

Analysis by gas chromatography mass spectrometry (GCMS) was performed on a QP2010 system (Shimadzu, Kyoto, Japan) equipped with a DB-5 column (5%-phenyl-methylpolysiloxane column; 30 m length, 0.25 mm ID, 0.25 µm film thickness; Agilent). Ionization was achieved by electron ionization (EI) at 70 eV. One microliter of the sample was injected using a splitless injector. The helium flow was set at 1.9 ml/min. The column temperature program began at 50°C, increased to 210°C at a rate of 35°C/min, and then increased to 280°C at a rate of 3°C/min. A mass spectrometer was set to unit mass resolution and three scans/s from m/z 37 to 700. Chromatograms and mass spectra were analyzed using GCMSsolution software (Shimadzu). For total CHC levels, the area under each of the CHC peaks were summed and normalized to the area under the peak for the spiked hexacosane standard. Statistical analysis was performed using a one-way ANOVA with post-hoc Holm-Sidak test.

REFERENCES

Acharya JK, Dasgupta U, Rawat SS, Yuan C, Sanxaridis PD, Yonamine I, Karim P, Nagashima K, Brodsky MH, Tsunoda S, Acharya U (2008). Cell-nonautonomous function of ceramidase in photoreceptor homeostasis. Neuron 57, 69–79.

Acharya U, Patel S, Koundakjian E, Nagashima K, Han X, Acharya JK (2003). Modulating sphingolipid biosynthetic pathway rescues photoreceptor degeneration. Science 299, 1740–1743.

Bilen J, Bonini NM (2005). Drosophila as a model for human neurodegenerative disease. Annu Rev Genet 39, 153–171.

Billeter JC, Atallah J, Krupp JJ, Millar JG, Levine JD (2009). Specialized cells tag sexual and species identity in Drosophila melanogaster. Nature 461, 987–991.

Brankatschk M, Eaton S (2010). Lipoprotein particles cross the blood-brain barrier in Drosophila. J Neurosci 30, 10441–10447.

Carvalho M, Sampaio JL, Palm W, Brankatschk M, Eaton S, Shevchenko A (2012). Effects of diet and development on the Drosophila lipidome. Mol Syst Biol 8, 600.

Carvalho M, Schwudke D, Sampaio JL, Palm W, Riezman I, Dey G, Gupta GD, Mayor S, Riezman H, Shevchenko A, et al. (2010). Survival strategies of a sterol auxotroph. Development 137, 3675–3685.

Cheng H, Wang M, Li JL, Cairns NJ, Han X (2013). Specific changes of sulfatide levels in individuals with pre-clinical Alzheimer's disease: an early event in disease pathogenesis. J Neurochem 127, 733–738.

Cutler RG, Kelly J, Storie K, Pedersen WA, Tammara A, Hatanpaa K, Troncoso JC, Mattson MP (2004). Involvement of oxidative stress-induced abnormalities in ceramide and cholesterol metabolism in brain aging and Alzheimer's disease. Proc Natl Acad Sci USA 101, 2070–2075.

Dasgupta U, Bamba T, Chiantia S, Karim P, Tayoun AN, Yonamine I, Rawat SS, Rao RP, Nagashima K, Fukusaki E, et al. (2009). Ceramide kinase regulates phospholipase C and phosphatidylinositol 4, 5, bisphosphate in phototransduction. Proc Natl Acad Sci USA 106, 20063–20068.

Dermaut B, Norga KK, Kania A, Verstreken P, Pan H, Zhou Y, Callaerts P, Bellen HJ (2005). Aberrant lysosomal carbohydrate storage accompanies endocytic defects and neurodegeneration in Drosophila benchwarmer. J Cell Biol 170, 127–139.

Ejsing CS, Sampaio JL, Surendranath V, Duchoslav E, Ekroos K, Klemm RW, Simons K, Shevchenko A (2009). Global analysis of the yeast lipidome by quantitative shotgun mass spectrometry. Proc Natl Acad Sci USA 106, 2136–2141.

Fergestad T, Olson L, Patel KP, Miller R, Palladino MJ, Ganetzky B (2008). Neuropathology in Drosophila mutants with increased seizure susceptibility. Genetics 178, 947–956.

Georgakopoulou EA, Tsimaratou K, Evangelou K, Fernandez Marcos PJ, Zoumpourlis V, Trougakos IP, Kletsas D, Bartek J, Serrano M, Gorgoulis VG (2013). Specific lipofuscin staining as a novel biomarker to detect replicative and stress-induced senescence. A method applicable in cryopreserved and archival tissues. Aging (Albany NY) 5, 37–50.

Ghosh A, Kling T, Snaidero N, Sampaio JL, Shevchenko A, Gras H, Geurten B, Gopfert MC, Schulz JB, Voigt A, Simons M (2013). A global in vivo Drosophila RNAi screen identifies a key role of ceramide phosphoethanolamine for glial ensheathment of axons. PLoS Genet 9, e1003980.

Gray DA, Woulfe J (2005). Lipofuscin and aging: a matter of toxic waste. Sci Aging Knowl Environ 2005, re1.

Guan XL, Cestra G, Shui G, Kuhrs A, Schittenhelm RB, Hafen E, van der Goot FG, Robinett CC, Gatti M, Gonzalez-Gaitan M, Wenk MR (2013). Biochemical membrane lipidomics during Drosophila development. Dev Cell 24, 98–111.

Gutierrez E, Wiggins D, Fielding B, Gould AP (2007). Specialized hepatocyte-like cells regulate Drosophila lipid metabolism. Nature 445, 275–280.

Han X, Rozen S, Boyle SH, Hellegers C, Cheng H, Burke JR, Welsh-Bohmer KA, Doraiswamy PM, Kaddurah-Daouk R (2011). Metabolomics in early Alzheimer's disease: identification of altered plasma sphingolipidome using shotgun lipidomics. PLoS One 6, e21643.

Hebbar S, Hall RE, Demski SA, Subramanian A, Fernandes JJ (2006). The adult abdominal neuromuscular junction of Drosophila: a model for synaptic plasticity. J Neurobiol 66, 1140–1155.

Hebbar S, Sahoo I, Matysik A, Argudo Garcia I, Osborne KA, Papan C, Torta F, Narayanaswamy P, Fun XH, Wenk MR, et al. (2015). Ceramides and stress signalling intersect with autophagic defects in neurodegenerative Drosophila blue cheese (bchs) mutants. Sci Rep 5, 15926.

Herzog R, Schwudke D, Schuhmann K, Sampaio JL, Bornstein SR, Schroeder M, Shevchenko A (2011). A novel informatics concept for high-throughput shotgun lipidomics based on the molecular fragmentation query language. Genome Biol 12, R8.

Hickey AJ, Chotkowski HL, Singh N, Ault JG, Korey CA, MacDonald ME, Glaser RL (2006). Palmitoyl-protein thioesterase 1 deficiency in Drosophila melanogaster causes accumulation of abnormal storage material and reduced life span. Genetics 172, 2379–2390.

Hindle S, Hebbar S, Sweeney ST (2011). Invertebrate models of lysosomal storage disease: what have we learned so far? Invert Neurosci 11, 59–71.

Hindle SJ, Hebbar S, Schwudke D, Elliott CJ, Sweeney ST (2017). A saposin deficiency model in Drosophila: lysosomal storage, progressive neurodegeneration and sensory physiological decline. Neurobiol Dis 98, 77–87.

Hoglinger D, Haberkant P, Aguilera-Romero A, Riezman H, Porter FD, Platt FM, Galione A, Schultz C (2015). Intracellular sphingosine releases calcium from lysosomes. Elife 4, e10616.

Hortsch R, Lee E, Erathodiyil N, Hebbar S, Steinert S, Lee JY, Chua DS, Kraut R (2010). Glycolipid trafficking in Drosophila undergoes pathway switching in response to aberrant cholesterol levels. Mol Biol Cell 21, 778–790.

Ito M, Masuda N, Shinomiya K, Endo K, Ito K (2013). Systematic analysis of neural projections reveals clonal composition of the Drosophila brain. Curr Biol 23, 644–655.

Jang S, Nelson JC, Bend EG, Rodriguez-Laureano L, Tueros FG, Cartagenova L, Underwood K, Jorgensen EM, Colon-Ramos DA (2016). Glycolytic enzymes localize to synapses under energy stress to support synaptic function. Neuron 90, 278–291.

Kawahara A, Nishi T, Hisano Y, Fukui H, Yamaguchi A, Mochizuki N (2009). The sphingolipid transporter spns2 functions in migration of zebrafish myocardial precursors. Science 323, 524–527.

Kumarasamy SK, Wang Y, Viswanathan V, Kraut RS (2008). Multivariate profiling of neurodegeneration-associated changes in a subcellular compartment of neurons via image processing. BioData Min 1, 10.

Lim A, Kraut R (2009). The Drosophila BEACH family protein, blue cheese, links lysosomal axon transport with motor neuron degeneration. J Neurosci 29, 951–963.

Liu L, Zhang K, Sandoval H, Yamamoto S, Jaiswal M, Sanz E, Li Z, Hui J, Graham BH, Quintana A, Bellen HJ (2015). Glial lipid droplets and ROS induced by mitochondrial defects promote neurodegeneration. Cell 160, 177–190.

Lloyd-Evans E, Morgan AJ, He X, Smith DA, Elliot-Smith E, Sillence DJ, Churchill GC, Schuchman EH, Galione A, Platt FM (2008). Niemann-Pick disease type C1 is a sphingosine storage disease that causes deregulation of lysosomal calcium. Nat Med 14, 1247–1255.

Matyash V, Liebisch G, Kurzchalia TV, Shevchenko A, Schwudke D (2008). Lipid extraction by methyl-tert-butyl ether for high-throughput lipidomics. J Lipid Res 49, 1137–1146.

Mi H, Lazareva-Ulitsky B, Loo R, Kejariwal A, Vandergriff J, Rabkin S, Guo N, Muruganujan A, Doremieux O, Campbell MJ, et al. (2005). The PANTHER database of protein families, subfamilies, functions and pathways. Nucleic Acids Res 33, D284–D288.

Milton VJ, Jarrett HE, Gowers K, Chalak S, Briggs L, Robinson IM, Sweeney ST (2011). Oxidative stress induces overgrowth of the Drosophila neuromuscular junction. Proc Natl Acad Sci USA 108, 17521–17526.

Nakano Y, Fujitani K, Kurihara J, Ragan J, Usui-Aoki K, Shimoda L, Lukacsovich T, Suzuki K, Sezaki M, Sano Y, et al. (2001). Mutations in the novel membrane protein spinster interfere with programmed cell death and cause neural degeneration in Drosophila melanogaster. Mol Cell Biol 21, 3775–3788.

Osborne N, Brand-Arzamendi K, Ober EA, Jin SW, Verkade H, Holtzman NG, Yelon D, Stainier DY (2008). The spinster homolog, two of hearts, is required for sphingosine 1-phosphate signaling in zebrafish. Curr Biol 18, 1882–1888.

Palm W, Sampaio JL, Brankatschk M, Carvalho M, Mahmoud A, Shevchenko A, Eaton S (2012). Lipoproteins in Drosophila melanogaster–assembly, function, and influence on tissue lipid composition. PLoS Genet 8, e1002828.

Panchal M, Gaudin M, Lazar AN, Salvati E, Rivals I, Ayciriex S, Dauphinot L, Dargere D, Auzeil N, Masserini M, et al. (2014). Ceramides and sphingomyelinases in senile plaques. Neurobiol Dis 65, 193–201.

Pantoja M, Fischer KA, Ieronimakis N, Reyes M, Ruohola-Baker H (2013). Genetic elevation of sphingosine 1-phosphate suppresses dystrophic muscle phenotypes in Drosophila. Development 140, 136–146.

Rohrbough J, Rushton E, Palanker L, Woodruff E, Matthies HJ, Acharya U, Acharya JK, Broadie K (2004). Ceramidase regulates synaptic vesicle exocytosis and trafficking. J Neurosci 24, 7789–7803.

Rong Y, McPhee CK, Deng S, Huang L, Chen L, Liu M, Tracy K, Baehrecke EH, Yu L, Lenardo MJ (2011). Spinster is required for autophagic lysosome reformation and mTOR reactivation following starvation. Proc Natl Acad Sci USA 108, 7826–7831.

Sampaio JL, Gerl MJ, Klose C, Ejsing CS, Beug H, Simons K, Shevchenko A (2011). Membrane lipidome of an epithelial cell line. Proc Natl Acad Sci USA 108, 1903–1907.

Sasamura T, Matsuno K, Fortini ME (2013). Disruption of Drosophila melanogaster lipid metabolism genes causes tissue overgrowth associated with altered developmental signaling. PLoS Genet 9, e1003917.

Schneider CA, Rasband WS, Eliceiri KW (2012). NIH Image to ImageJ: 25 years of image analysis. Nat Methods 9, 671–675.

Schwudke D, Schuhmann K, Herzog R, Bornstein SR, Shevchenko A (2011). Shotgun lipidomics on high resolution mass spectrometers. Cold Spring Harb Perspect Biol 3, a004614.

Seppo A, Moreland M, Schweingruber H, Tiemeyer M (2000). Zwitterionic and acidic glycosphingolipids of the Drosophila melanogaster embryo. Eur J Biochem 267, 3549–3558.

Shevchenko A, Simons K (2010). Lipidomics: coming to grips with lipid diversity. Nat Rev Mol Cell Biol 11, 593–598.

Shevchenko A, Tomas H, Havlis J, Olsen JV, Mann M (2006). In-gel digestion for mass spectrometric characterization of proteins and proteomes. Nat Protoc 1, 2856–2860.

Starostina E, Xu A, Lin H, Pikielny CW (2009). A Drosophila protein family implicated in pheromone perception is related to Tay-Sachs GM2-activator protein. J Biol Chem 284, 585–594.

Stern CA, Braverman TR, Tiemeyer M (2000). Molecular identification, tissue distribution and subcellular localization of mST3GalV/GM3 synthase. Glycobiology 10, 365–374.

Sweeney ST, Davis GW (2002). Unrestricted synaptic growth in spinster-a late endosomal protein implicated in TGF-beta-mediated synaptic growth regulation. Neuron 36, 403–416.

te Vruchte D, Lloyd-Evans E, Veldman RJ, Neville DC, Dwek RA, Platt FM, van Blitterswijk WJ, Sillence DJ (2004). Accumulation of glycosphingolipids in Niemann-Pick C disease disrupts endosomal transport. J Biol Chem 279, 26167–26175.

Thomas PD, Campbell MJ, Kejariwal A, Mi H, Karlak B, Daverman R, Diemer K, Muruganujan A, Narechania A (2003). PANTHER: a library of protein families and subfamilies indexed by function. Genome Res 13, 2129–2141.

Venkatachalam K, Long AA, Elsaesser R, Nikolaeva D, Broadie K, Montell C (2008). Motor deficit in a Drosophila model of mucolipidosis type IV due to defective clearance of apoptotic cells. Cell 135, 838–851.

Xu Y, Condell M, Plesken H, Edelman-Novemsky I, Ma J, Ren M, Schlame M (2006). A Drosophila model of Barth syndrome. Proc Natl Acad Sci USA 103, 11584–11588.

Yew JY, Chung H (2015). Insect pheromones: An overview of function, form, and discovery. Prog Lipid Res 59, 88–105.

Zigdon H, Kogot-Levin A, Park JW, Goldschmidt R, Kelly S, Merrill AH Jr, Scherz A, Pewzner-Jung Y, Saada A, Futerman AH (2013). Ablation of ceramide synthase 2 causes chronic oxidative stress due to disruption of the mitochondrial respiratory chain. J Biol Chem 288, 4947–4956.